Structure Tensor Based Analysis of Cells and Nuclei Organization in Tissues

Wenxing Zhang, Jérôme Fehrenbach, Annaïck Desmaison, Valérie Lobjois, Bernard Ducommun, and Pierre Weiss*

Abstract—**Extracting geometrical information from large 2D or 3D biomedical images is important to better understand fundamental phenomena such as morphogenesis. We address the problem of automatically analyzing spatial organization of cells or nuclei in 2D or 3D images of tissues. This problem is challenging due to the usually low quality of microscopy images as well as their typically large sizes. The structure tensor is a simple and robust descriptor that was developed to analyze textures orientation. Contrarily to segmentation methods which rely on an object based modeling of images, the structure tensor considers the sample at a macroscopic scale, like a continuous medium. We show that this tool allows quantifying two important features of nuclei in tissues: their privileged orientation as well as the ratio between the length of their main axes. A quantitative evaluation of the method is provided for synthetic and real 2D and 3D images. As an application, we analyze the nuclei orientation and anisotropy on multicellular tumor spheroids cryosections. This analysis reveals that cells are elongated in a privileged direction that is parallel to the spheroid boundary. A MATLAB toolbox and an Icy plugin are available to use the proposed method.**

Index Terms—**Biomedical image analysis, structure tensor, cells and nuclei.**

I. INTRODUCTION

T HE advent of new imaging technologies allows observing biological samples with an unprecedented spatial, temporal and spectral resolution. It offers new opportunities to perform systematic studies of geometrical configurations of cells or nuclei in their micro-environment to better understand the fundamental processes involved in morphogenesis or tumor growth [22], [30].

Automatic procedures are however essential to analyze large images and assess cells properties such as location, size, orientation, aspect ratio, etc. The lack of robust, fast and universal procedures to provide such a geometric description is probably one of the main obstacles to exploit the full potential of new devices.

A standard approach to analyze image contents consists of *segmenting* each cell/nucleus independently [30], [33]. A precise segmentation completely describes the geometrical contents of images and is often regarded as the best source of information one can hope for. However, biological images often suffer from many degradations. For instance, in fluorescence microscopy, light scattering, absorption or poor signal-to-noise-ratio strongly impair image quality. In many situations it is therefore hopeless to perform a proper segmentation. Moreover, in cases where large cell populations are investigated, a complete segmentation (i.e., a precise description of the objects boundaries) still brings more information than needed to understand the overall geometrical distribution.

    a) Contribution: In this paper we therefore pursue a less ambitious goal. We adopt a macroscopic point of view and consider the biological sample as a continuous medium. This idea stems from mathematical models that describe tissues as continuous media such as incompressible fluids, elastic or viscoelastic materials [1], [3], [5], [18], [19]. Our main contribution is to show through both theoretical and numerical results that the so-called *structure tensor* [2], [14], [15], provides a robust and precise enough method to retrieve cells orientation and anisotropy in 2D and in 3D. In addition, the structure tensor can be evaluated very fast and only requires tuning one parameter. We show the following original results:

- While the structure tensor is usually implemented to assess texture orientations, we show that it also allows quantifying the anisotropy of cells or nuclei. This is done by analyzing the method behavior on images with ellipsoidal isosurfaces. To the best of our knowledge, this is the first theoretical result that allows exploiting the structure tensor eigenvalues in a precise way.
- The structure tensor only requires tuning one parameter. We show that it suffices to set it equal to the typical size of a cell in pixels.
- The proposed mathematical analysis also allows quantifying the method bias. It shows that a very good estimation

W. X. Zhang is with CNRS, ITAV-USR3505 and Université de Toulouse, ITAV-USR3505, 31500 Toulouse, France, and also with the School of Mathematical Sciences, University of Electronic Science and Technology of China, 61000 Chengdu, China.

J. Fehrenbach is with CNRS, ITAV-USR3505 and Université de Toulouse, ITAV-USR3505, 31500 Toulouse, France, and also with the CNRS, IMT-UMR5219, and Université de Toulouse, IMT-UMR5219, 31500 Toulouse, France.

A. Desmaison and V. Lobjois are with CNRS, ITAV-USR3505 and Université de Toulouse, ITAV-USR3505, 31500 Toulouse, France.

B. Ducommun is with CNRS, ITAV-USR3505 and Université de Toulouse, ITAV-USR3505, 31500 Toulouse, France and also with CHU de Toulouse, 31500 Toulouse, France.

*P. Weiss is with CNRS, ITAV-USR3505 and Université de Toulouse, ITAV-USR3505, 31106 Toulouse, France, and also with the CNRS, IMT-UMR5219, and Université de Toulouse, IMT-UMR5219, 31106 Toulouse, France (e-mail: pierre.armand.weiss@gmail.com).

can be expected even when very few nuclei are locally similar (in the sense that they can be well approximated by the same ellipsoid).

- We prove that the method is invariant under contrast changes and robust to deformations and noise.

We also perform various experiments to validate our theoretical findings. We assess the structure tensor efficiency on synthetic and real 2D and 3D images. Its output is compared to ground truth obtained analytically in the case of synthetic data or manually in the case of real data. This analysis shows that the structure tensor allows to quickly and robustly assess cells organization at a large scale. We also perform a comparison with the output of standard 2D segmentation algorithms: FarSight [27], the HK-means plugin from Icy [9], [33], the "IdentifyPrimaryObjects" routine from Cellprofiler [7] and MINS [25]. The structure tensor provides significantly better estimates of orientation and anisotropy than all tested methods. We finish the paper by providing an example of application to the analysis of geometrical configurations of nuclei in multicellular tumor spheroids.

The source codes allowing to reproduce our experiments are available in MATLAB at http://www.math.univ-toulouse.fr/~weiss/PageCodes.html. We also developed two Icy plugins [9] for this project. The first one allows to manually fit ellipses on 2D images to generate gold standards. The second one implements the structure tensor and allows visualizing its output in 2D and 3D. Both plugins are available in the official list of Icy plugins.

b) Related Work: The structure tensor appeared in the field of image processing in the late 80's [14] for the problem of interest point detection. It was then justified theoretically and popularized in different contexts such as interest point detection [14], [17], [24], texture analysis [2], [15], representation of flow-like images [34], optical flow problems [26] and anisotropic or coherence enhancing diffusion [43], [44]. The structure tensor is described precisely in standard textbooks [20], [21], [43] and sometimes referred to as second moment matrix [23]. The works [2], [15], [34] are closely related to ours since the authors show that the structure tensor is capable of assessing precisely the orientation of textures composed of segments or step functions. In this paper, we demonstrate that the structure tensor is capable of retrieving the orientation of another type of functions, but we also precisely analyze the meaning of the eigenvalues ratio. To the best of our knowledge, this is the first result in this direction.

The structure tensor has already been used in the specific field of biological imaging. One of its main applications is coherence enhancing or diffusion [33] which usually allows improving images quality without degrading their geometrical content severely. It was also used to analyze geometrical features such as fibers orientations in 2D and 3D [11], [13], [28], [31], [35]. The works [13], [35] also come with an ImageJ plugin http://bigwww.epfl.ch/demo/orientation/. The authors of these two references mention that the structure tensor allows quantifying the orientation and the isotropy properties of a region of interest. However, the isotropy is defined in a way different from the present paper and the authors do not state precisely how this information relates to the image contents.

c) Paper Contents: The rest of the paper is organized as follows. Section II constitutes the theoretical part of the paper. We introduce the structure tensor and demonstrate its properties when applied to images that consist of fields of functions with ellipsoidal isosurfaces. We validate our main theoretical findings with specific numerical experiments on synthetic data. In Section III, we turn to the real problem of assessing cells configurations in a dense tissue. We first illustrate the method on synthetic 2D and 3D data with controlled degradations and finally propose results on real 2D images of tumor spheroids.

II. THEORETICAL AND EMPIRICAL ANALYSIS

In this section, we first recall the structure tensor definition in $\mathbb{R}^d$. Second, we provide a numerical algorithm to compute it in the discrete setting. We then show its ability to analyze fields of ellipses (in 2D) or ellipsoids (in 3D). The motivation for introducing fields of functions with ellipsoidal isosurfaces is that images such as Fig. 6 are a rather good approximation of certain dense tissues such as microtumors. We then show that the method is robust to deformations. We finish by illustrating the theoretical results with numerical experiments.

A. Notation

For $\mathbf{x}, \mathbf{y} \in \mathbb{R}^d$, the angle in degrees between $\mathbf{x}$ and $\mathbf{y}$ is denoted $\angle(\mathbf{x}, \mathbf{y})$, this angle lies in $(0°, 90°)$. The ℓ^p-norm of $\mathbf{x} = (x_1, \ldots, x_d) \in \mathbb{R}^d$ is denoted $\|\mathbf{x}\|_p$ and defined by $\|\mathbf{x}\|_p := (\sum_{i=1}^{d} |x_i|^p)^{1/p}$. The L^p-norm $(p < +\infty)$ of a function $f : \mathbb{R}^d \to \mathbb{R}$ is denoted $\|f\|_p$ and defined by $\|f\|_p := (\int_{\mathbb{R}^d} |f(\mathbf{x})|^p d\mathbf{x})^{1/p}$. The L^∞-norm is defined by $\|f\|_\infty := \sup_{\mathbf{x} \in \mathbb{R}^d} |f(\mathbf{x})|$. Let $G : \mathbb{R}^d \to \mathbb{R}^d$ denote a vector field, we let DG denote its gradient and $\|G\|_{W^{1,\infty}} := \sup_{\mathbf{x} \in \mathbb{R}^d} \|DG(\mathbf{x})\|_2 + \|G(\mathbf{x})\|_2$. The positive definiteness of a matrix A is denoted $A \succ 0$. The spectral norm of a matrix A is denoted $\|A\|_2$, and its determinant is denoted $|A|$. We denote $\bar{A} := A/\|A\|_2$ the normalized version of A. The largest (resp. smallest) eigenvalue of A is denoted $\lambda_{\max}(A)$ (resp. $\lambda_{\min}(A)$). The notation Id denotes the identity operator. $M \propto N$ means that the matrices M and N are proportional, and $f \propto g$ means that the functions f and g are proportional. Given a vector $\mathbf{x} \in \mathbb{R}^d$, we let $\text{diag}(\mathbf{x})$ denote a diagonal matrix with diagonal $\mathbf{x}$. The support of a function ψ is the closure of the set where this function does not vanish and is denoted $\text{supp}(\psi)$. A function is of class $\mathcal{C}^1$ if it is continuously differentiable and $L^1(\mathbb{R}^d)$ denotes the set of integrable function on $\mathbb{R}^d$.

B. Preliminary Facts About the Structure Tensor

Let $u : \mathbb{R}^d \to \mathbb{R}$ denote a grayscale image. In this paper, we restrict to the practical cases $d = 2$ and $d = 3$, although the theory is valid in any dimension. For ease of exposition, we assume that $u \in \mathcal{C}^1(\mathbb{R}^d)$ has bounded partial derivatives. The function $K \in L^1(\mathbb{R}^d)$ is a filter that satisfies the following conditions:

$$(i) \ K(\mathbf{x}) \geq 0, \ \forall \mathbf{x} \in \mathbb{R}^d; \ (ii) \int_{\mathbb{R}^d} K(\mathbf{x}) \, d\mathbf{x} = 1. \quad (1)$$

For any $\rho > 0$, we define K_ρ, the scaled version of K by

$$K_\rho(\mathbf{x}) := \frac{1}{\rho^d} K\left(\frac{\mathbf{x}}{\rho}\right), \quad \forall \mathbf{x} \in \mathbb{R}^d. \tag{2}$$

The conditions (1) still hold for any $\rho > 0$. In practice, K is usually a smoothing filter (e.g., a Gaussian). The structure tensor of u, denoted J_ρ, is defined by

$$J_\rho := K_\rho \star (\nabla u \nabla u^T), \tag{3}$$

where ∇ denotes the gradient operator and '$\star$' is the convolution operation which acts independently on each component of the $d \times d$ tensor $\nabla u \nabla u^T$.

C. Discretization and Numerical Implementation

In order to implement the structure tensor on a digital image, the differential operators have to be discretized. The discrete gradient operator ∇ is defined by $\nabla = \begin{pmatrix} \partial_1 \\ \vdots \\ \partial_d \end{pmatrix}$. In all reported experiments, the partial differential operators ∂_i are defined as convolutions with discrete kernels. From an asymptotic point of view any kernel leading to a consistent discretization should provide good results. However, the kernel design turns out to be crucial to provide good orientation and anisotropy estimates. Key properties of discrete kernels are [20], [37], [45]: i) *consistency*, to ensure a proper estimation of the gradient ii) *rotation invariance*, ensuring a reliable orientation estimation and iii) *no shift*, implying the use of centered finite differences. Additionnally it can be helpful to satisfy *separability* which ensures faster computations. Following these criteria, the authors of [37], [45] designed the following filter in 2D:

$$h = \frac{1}{32} \begin{pmatrix} -3 & 0 & 3 \\ -10 & 0 & 10 \\ -3 & 0 & 3 \end{pmatrix}$$

and proposed to set $\partial_1 u = h \star u$ and $\partial_2 u = h^T \star u$. Using the same methodology in 3D, one can derive the following filter (using MATLAB notation):

$$h(:,:,1) = \begin{pmatrix} 0.0153 & 0 & -0.0153 \\ 0.0568 & 0 & -0.0568 \\ 0.0153 & 0 & -0.0153 \end{pmatrix},$$

$$h(:,:,2) = \begin{pmatrix} 0.0568 & 0 & -0.0568 \\ 0.2117 & 0 & -0.2117 \\ 0.0568 & 0 & -0.0568 \end{pmatrix}$$

and $h(:,:,3) = h(:,:,1)$.

Alternative discretizations could be used. For instance, it is possible to use wider stencils to improve rotation invariance. Another possibility is to directly define kernels through their discrete Fourier decomposition. This ensures the best possible rotation invariance, but slows down computations since it requires using Fast Fourier Transforms (FFTs). In this paper, we stick to the 3×3 kernel described above since we observed that it provides good enough results in applications.

Finally, let us mention that the structure tensor can easily handle non isotropic pixels. This is important since very often in imaging, the z-direction has a lower resolution than the xy-plane. By letting $\Delta_1, \ldots, \Delta_d$ denote the pixels widths in each direction, it suffices to normalize the filter for the i-th direction by a factor $(1)/(\Delta_i)$.

The gradient is computed in the space domain, while the convolution with K_ρ is based on FFTs. The overall computational complexity for an image with n pixels is therefore $\mathcal{O}(n \log(n))$. In practice, the structure tensor can be considered as a very elementary tool and computed rapidly for most images. It can also be easily parallelized on multicore or GPU architectures. Parts of the Icy plugin we developed are multi-threaded.

D. Structure Tensor and a Single Ellipsoid

In this section, we analyze the structure tensor behavior on a simple image with isosurfaces that are concentric ellipsoids. We show that it allows recovering its principal orientations as well as the ratios between the lengths of the ellipsoid main axes.

Let $\varphi : \mathbb{R}_+ \to \mathbb{R}$ denote a $\mathcal{C}^1$ function different from 0 satisfying $\varphi'(0) = 0$. Let $A = U\Sigma U^T \in \mathbb{R}^{d \times d}$ denote a symmetric positive-definite matrix where $\Sigma = \text{diag}(\sigma_1^{-2}, \ldots, \sigma_d^{-2})$ and U is orthogonal. Define $\psi : \mathbb{R}^d \to \mathbb{R}$ by

$$\psi(\mathbf{x}) := \varphi(\mathbf{x}^T A \mathbf{x}), \quad \forall \mathbf{x} \in \mathbb{R}^d. \tag{4}$$

The isosurfaces of ψ are ellipsoids in $\mathbb{R}^d$ with semiaxes of length $\sigma_i (i = 1, 2, \ldots, d)$.

Proposition 1: Let $u := \psi$ with ψ defined in (4). Assume that $\text{supp}(\psi) \subset [-(1)/(2), (1)/(2)]^d$. Let K be the indicator of a unit disk:

$$K(\mathbf{x}) = \begin{cases} C_d, & \text{if } \|\mathbf{x}\|_2 \leq 1; \\ 0, & \text{otherwise,} \end{cases} \tag{5}$$

where the normalizing constant C_d is chosen so that the normalization condition (ii) of (1) is satisfied. Then, for all $\rho \geq \sqrt{d/2}$, we have $\bar{J}_\rho(0) = \bar{A}$ and if $\mathbf{x}$ is small enough then $\bar{J}_\rho(\mathbf{x}) = \bar{J}_\rho(0)$.

See Appendix B.A for the proof. This proposition leads to the following observations:

- First, for simple functions with ellipsoidal isosurfaces, a diagonalization of the structure tensor allows recovering the orientation matrix U as well as the matrix Σ up to a multiplicative constant. In 2D, it means that $\sqrt{\lambda_{\min}(J_\rho(0))/\lambda_{\max}(J_\rho(0))}$ corresponds exactly to the ratio between the principal axes.
- Second, since this result holds for *any* function φ, the method is *contrast invariant*, which is a highly desirable property. Contrast invariance basically indicates that the method should behave similarly on different imaging devices or when using different stainings.
- Third, the structure tensor is *stable*, in the sense that this result holds not only at point 0, but also in a neighborhood of 0.

E. Structure Tensor and Fields of Ellipsoids

In the previous section, we focussed on a very simple image model. We now turn to a slightly more realistic setting where u is the sum of functions with ellipsoidal isosurfaces and nonoverlapping supports.
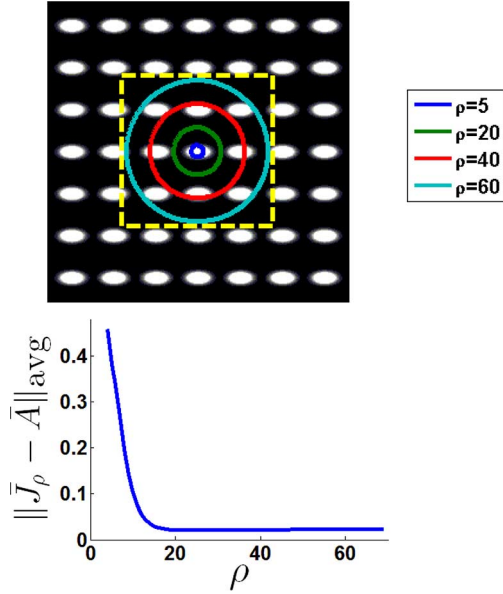
Fig. 1. Top: image u defined in (6). The size of test image is 256×256. The semi-axes lengths of a single ellipsoid are respectively 8 and 4 pixels. Bottom: $\|\bar{J}_\rho(\mathbf{x}) - \bar{A}\|_{\text{avg}}$ w.r.t. ρ. The quantity $\|\bar{J}_\rho(\mathbf{x}) - \bar{A}\|_{\text{avg}}$ is the average error within a 128×128 window (dashed line in clean image).

We use the same notation as in the previous section and assume that $\text{supp}(\psi) \subset [-(1)/(2), (1)/(2)]^d$. The Dirac comb, denoted by III, is defined by

$$\text{III} := \sum_{\mathbf{x} \in \mathbb{Z}^d} \delta_{\mathbf{x}},$$

where $\delta_{\mathbf{x}}$ is the Dirac delta function (see e.g., [4]). Consider the image u

$$u = \text{III} \star \psi, \tag{6}$$

where ψ is defined in (4). The image u consists of a function ψ replicated periodically over all $\mathbb{R}^d$. Note that the translated versions of ψ do not overlap since $\text{supp}(\psi) \subset [-(1)/(2), (1)/(2)]^d$. Fig. 1 illustrates such an image in the 2D case.

Proposition 1 indicates that $J_\rho(0)$ allows retrieving the orientation and anisotropy of u. However, that proposition holds under the following assumptions: (i) the image u has concentric ellipsoidal isosurfaces, (ii) the ellipsoid's center should be known. Both requirements are hardly met in practical applications. The questions we tackle in this paragraph are the following: does the structure tensor provide an approximation of $\bar{A}$ at any point of the image domain? How many cells are necessary to reach a low approximation error?

The following proposition provides a preliminary answer.

Proposition 2: Let K be the function defined in (5) and u be the image defined in (6). Then $\|\bar{J}_\rho(\mathbf{x}) - \bar{A}\|_2 = O(1/\rho)$ for all $\mathbf{x} \in \mathbb{R}^d$.

See Appendix B.B for the proof. Proposition 2 indicates that $\bar{J}_\rho(\mathbf{x}) \simeq \bar{A}$ for any $\mathbf{x} \in \mathbb{R}^d$ and sufficiently large ρ. However, the asymptotic $O(1/\rho)$ convergence rate is not compelling. The following theorem shows that much better results can be obtained by using smoother kernels.

Theorem 1: Let K be the Gaussian function

$$K(\mathbf{x}) = \frac{1}{(2\pi)^{d/2}} \exp\left(-\frac{\|\mathbf{x}\|_2^2}{2}\right) \tag{7}$$

and u be the image defined in (6). Then there exists a constant $C > 0$ such that $\forall \rho \geq (1)/(2)$ and $\forall \mathbf{x} \in \mathbb{R}^d$:

$$\|\bar{J}_\rho(\mathbf{x}) - \bar{A}\|_2 \leq C \exp\left(-\frac{\rho^2}{2}\right).$$

See Appendix B.C for the proof. Surprisingly, the convergence of $\bar{J}_\rho(\mathbf{x})$ to $\bar{A}$ is extremely fast if smooth filters are used. Theorem 1 implies that values of ρ of the order of nuclei sizes should produce satisfactory orientation and anisotropy estimates. This will be confirmed in the numerical experiments, see Section III. A closer inspection at the proof of Theorem 1 reveals that the smoothness of the filter function plays a key role to control the asymptotic convergence rate.

Theorem 1 is illustrated in the 2D case in Fig. 1. The convergence rate is evaluated using the average of the spectral norm $\|\bar{J}_\rho(\mathbf{x}) - \bar{A}\|_2$ on a 128×128 window. The resulting average is denoted $\|\bar{J}_\rho - \bar{A}\|_{\text{avg}}$. It shows that the magnitude $\|\bar{J}_\rho - \bar{A}\|_{\text{avg}}$ decreases to zero (up to numerical errors) extremely fast. An ellipse is around 20 pixels wide and a value of ρ around 15 provides results nearly as good as can be expected.

To the best of our knowledge, Theorem 1 is the first theoretical result that shows that the structure tensor can be used not only for orientation estimation, but also for *anisotropy* estimation. Until now, the structure tensor was only analyzed using directed patterns such as segments [34] or step functions [2]. This result therefore sheds a new light on this fundamental tool.

F. Stability to Noise

In this paragraph, we show that the structure tensor is stable to noise, provided that adapted pre-processing is used. The structure tensor definition given in (3) is different from what is found in most textbooks [43], [44], where the image u is pre-convolved with a Gaussian filter in order to improve the signal-to-noise-ratio (SNR). Let us illustrate the detrimental effect of this strategy.

Assume for simplicity that $u = \psi$ and that $\varphi(t) = \exp(-t/2)$. The image $u(\mathbf{x}) = \exp(-\mathbf{x}^T A \mathbf{x}/2)$ is thus a Gaussian function with covariance matrix A^{-1}. If u is further convolved with a Gaussian filter as in [43], [44], we obtain

$$u_\sigma := K_\sigma \star u,$$

where K is the Gaussian filter defined in (7). By exploiting the facts that the convolution of Gaussian functions is still a Gaussian with covariance matrix equal to the sum of covariance matrices, we obtain

$$u_\sigma(\mathbf{x}) \propto \exp\left(-\frac{\mathbf{x}^T (A^{-1} + \sigma^2 \text{Id})^{-1} \mathbf{x}}{2}\right),$$

where Id is identity matrix. Consequently, pre-convolving u with a Gaussian filter shifts the eigenvalues of A^{-1} by a quantity σ^2. This, in turn, results in biased anisotropy estimates. For

instance, in the 2D case, the structure tensor based anisotropy obtained using u_σ is

$$\left(\frac{\lambda_{\max}^{-1}(A) + \sigma^2}{\lambda_{\min}^{-1}(A) + \sigma^2} \right)^{1/2},$$

which is different from the ground truth anisotropy $((\lambda_{\min}(A))/(\lambda_{\max}(A)))^{1/2}$. In other words the blurring tends to reduce the anisotropy. This effect is illustrated on the 3rd row of Fig. 3: the isotropic blur makes the ellipses rounder.

The simple analysis above shows that in practice, more advanced image denoising techniques that keep isosurfaces unchanged should be preferred over a simple convolution with a Gaussian filter. A wide choice is now available such as anisotropic diffusion, total variation denoising, frame based regularization or non-local methods [6], [8], [36], [39], [41].

Let us compare some of these methods. We present comparisons on a synthetic image perturbed by noise in Fig. 2. The image is denoised using three different methods: convolution by a Gaussian filter, total variation denoising [36] and BM3D [8]. For each of these three methods we evaluate the convergence rate of the estimated tensor to the ground truth. We present for comparison the convergence curve associated to the clean image. It can be noted that the image denoised using BM3D leads to results nearly as good as if the image was not perturbed by noise.

G. Stability to Deformations

The models we proposed until now are only rough approximations of real images and one may wonder whether the results obtained so far can be applied to real images. In this paragraph, we provide a positive answer to this question. We show that the structure tensor is robust, in the sense that small deformations of the image do not change its values significantly.

Theorem 2: Let u be an image such that ∇u is Lipschitz and let F be a diffeomorphism close to the identity, in the sense that $F = Id + G$ where $\|G\|_{W^{1,\infty}} \leq \eta$. The scale ρ is fixed. We let J denote the structure tensor associated to the image u and J' the structure tensor associated to the deformed image $u' = u \circ F$. Then

$$\|J' - J\|_\infty = O(\eta),$$

and thus $J'(\mathbf{x}) \to J(\mathbf{x})$ when $\eta \to 0$, uniformly in $\mathbf{x}$.

This theorem is proved in Appendix B.D.

H. An Experimental Stability Analysis

To finish this section, we propose to empirically analyse the robustness of the structure tensor to various degradations, namely: noise, anisotropy, blur, texture, deformation and subsampling. We perform experiments in 2D.

In all the experiments apart from the one related to resolution, we process images of size 256×256 composed of 8×8 synthetic cells, obtained by perturbing the image in Fig. 1. In all experiments, we set ρ equal to the size of a cell. Apart from the anisotropy experiment, we fix the ratio between the short and long axis of the ellipses to 1/2. The parameters used for each experiment are as follows:

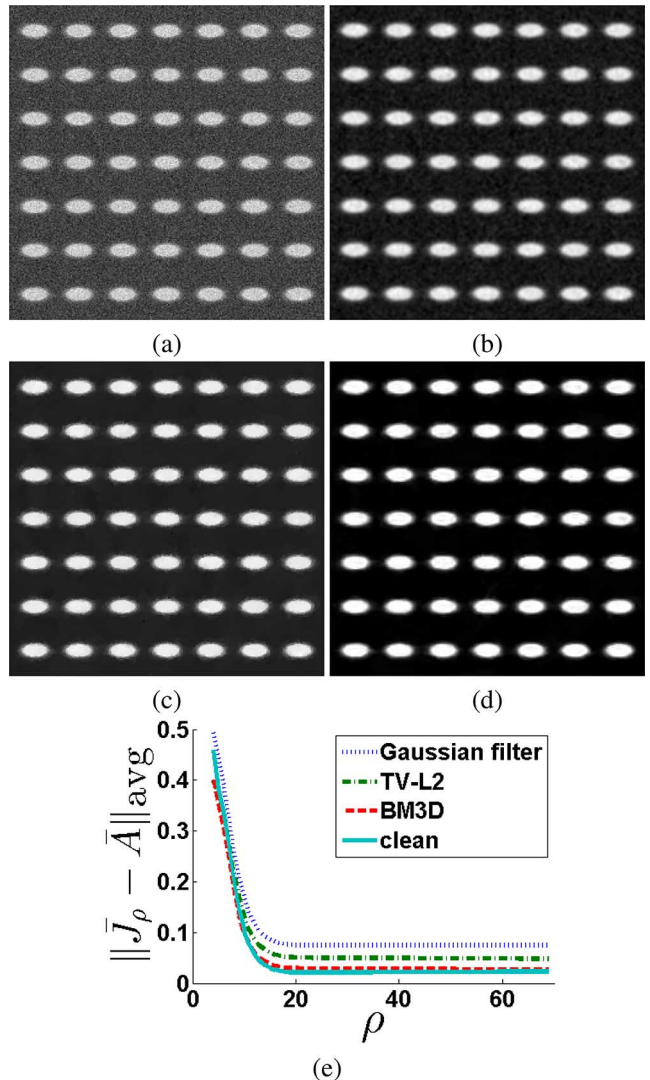(a)   (b)

(c)   (d)

(e)

Fig. 2. Experiment on a noisy image: (a) noisy image, (b) denoised image using convolution by a Gaussian kernel, (c) denoised image using total variation, (d) denoised image using BM3D, (e) evolution of the error in the estimated anisotropy tensor with respect to the radius of the kernel.

- *Noise:* we add Gaussian white noise to the synthetic image in Fig. 1. The SNRs of the noisy images vary from 67 dB (mild) to -8 dB (severe). The structure tensor is completely unstable to noise since it requires the evaluation of derivatives. We therefore denoise the image first using the BM3D algorithm.
- *Anisotropy:* we let the anisotropy vary between 1 (mild) to 1/10 (severe). This is not properly speaking a degradation, but allows to show that the method works fine even for very elongated cells.
- *Blur:* we generate an isotropic Gaussian blur with standard deviations varying from 0 (mild) to 10 pixels (severe).
- *Texture:* we add a random stationary texture defined by $b = \sum_{i=1}^{3} b_i \star K_{\alpha_i}$, where $b_i \sim \mathcal{N}(0, \sigma^2 I)$ and $\alpha_1 = 2, \alpha_2 = 4$ and $\alpha_3 = 8$. The variance σ^2 is varied to reach different SNRs ranging from 84 dB (mild) to 4 dB (severe). This definition allows testing the robustness to textures with different frequency components. In this case, we perform no denoising.
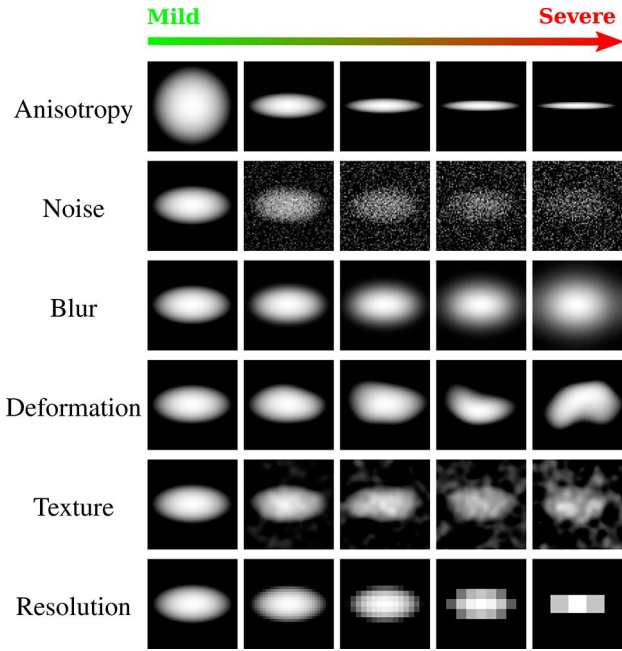
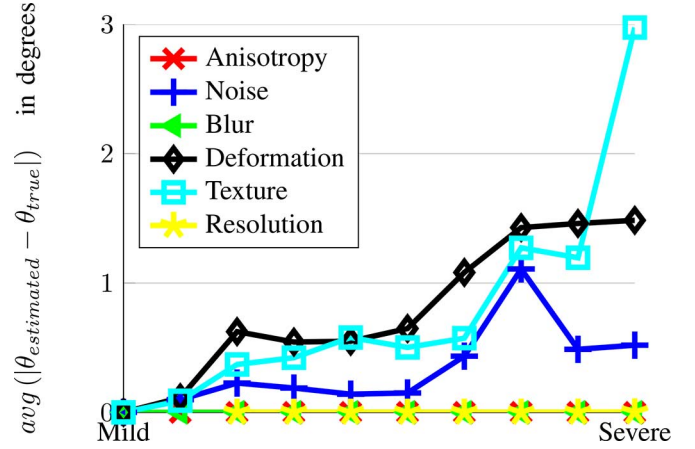Fig. 3.   Illustration of one cell with various degradations.

Fig. 4.   Robustness of the structure tensor in terms of orientation. Mean orientation error in degrees over a region containing 4 cells.
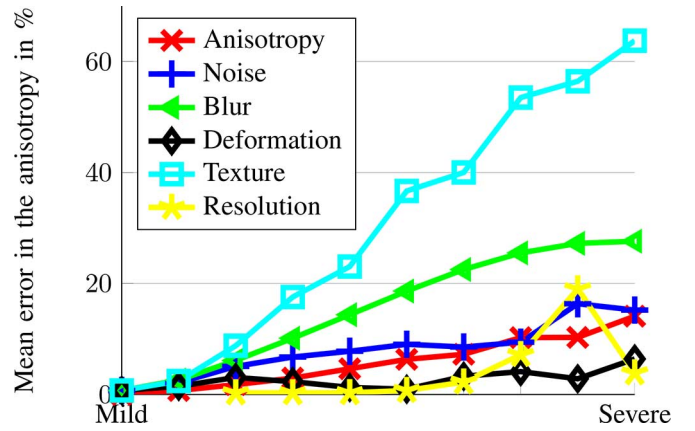

Fig. 5.   Robustness of the structure tensor in terms of anisotropy. Mean anisotropy error in % over a region containing 4 cells.

- *Deformation:* we generate random diffeomorphisms with maximal pixelwise displacement varying from 0 pixels (mild, no deformation) to 15 pixels (severe). To define the diffeomorphism, we generate a random Gaussian vector field with i.i.d. components. We then smooth it with an isotropic Gaussian of variance 10. Finally, we normalize it so that the maximum displacement is fixed. This experiment allows illustrating and validating Theorem 2.
- *Resolution:* we test different image resolutions. A cell resolution varies from 4×4 pixels (severe, the cell is represented by 3 non-zeros pixels) to 512×512 pixels (mild). We use a dyadic scale.

The different degradations are illustrated in Fig. 3. We only display a single cell due to space limitations. To measure the robustness, we evaluate two criteria: the mean orientation mismatch in degrees and the anisotropy mismatch in percents. The anisotropy mismatch is computed as follows. Let α denote the true anisotropy defined as the ratio between the smallest and the largest axis of the ellipses. Let $\tilde{\alpha}(\mathbf{x}) = \sqrt{(\lambda_{\min}(A(\mathbf{x})))/(\lambda_{\max}(A(\mathbf{x})))}$ denote the estimated anisotropy at point $\mathbf{x}$. The quality measure we propose is defined by:

$$E(\mathbf{x}) = 100 \cdot \left(\max\left(\frac{\alpha}{\tilde{\alpha}(\mathbf{x})}, \frac{\tilde{\alpha}(\mathbf{x})}{\alpha} \right) - 1 \right).$$

This measures how many times the estimated anisotropy is far away from the true anisotropy. A value of 0% is perfect while a value of 100% means that the estimated anisotropy is twice too large or too small.

The graph in Fig. 4 shows the mean error of orientation with respect to the degradation level. As can be seen, the orientation is accurately estimated for all types of degradation. The maximum error is 3 degrees.

The graph in Fig. 5 shows the mean error of anisotropy with respect to the degradation level. The results indicate that the

structure tensor is robust to deformation, noise, anisotropy and resolution since the error does not exceed 20% even in very degraded cases. This result is in some sense surprising: after deformation for instance, the anisotropy may have changed significantly, but the structure tensor retrieves the right value. The main reason is that the structure tensor averages the information from different cells, making it very stable.

The situation for texture and blur is not as good since the merit function is significantly higher. The blur was already shown to result in a biased estimation of the anisotropy in paragraph (II.F). As can be seen on the "Blur" row in Fig. 5, this behavior is quite natural: the severely blurred ellipse (right) is significantly less anisotropic than the mild one (left). The structure tensor can therefore not recover an accurate anisotropy estimate. Note that a segmentation estimate would probably suffer from the same bias. Deblurring algorithms are therefore crucially needed in heavily blurred images.

The addition of textures results in large errors. The main reason for this poor behavior is the presence of high frequency oscillations, which are essentially related to the noise component with $\alpha_1 = 2$. These oscillations make the gradient estimates inaccurate. This results in strong biases. The best solution to avoid this behavior would be to remove high frequency
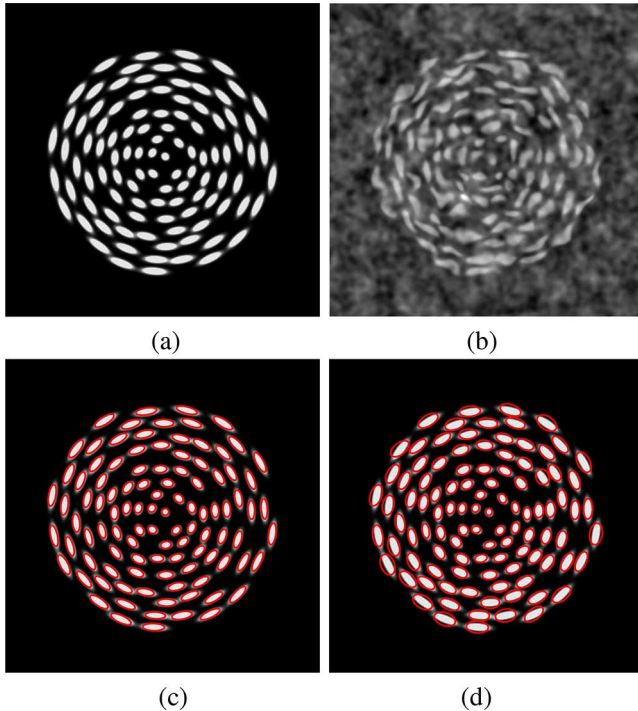
Fig. 6. Evaluation of the structure tensor on a 2D synthetic spheroid. (a) 512 × 512 clean synthetic tumor spheroid. (b) Degraded synthetic spheroid. (c) Structure tensor based analysis of the spheroid on the clean image. (d) Structure tensor based analysis of the spheroid on the degraded image. Note that in this case, we plot the ellipses on the clean image to ease the visualization. (a) Clean, (b) Degraded, SNR = 1.8 dB, (c) Recovered from clean, (d) Recovered from degraded.

textures prior to analysis. This can be achieved using dedicated methods for colored noise, see e.g., [12].

Overall, these experiments illustrate the stability of the structure tensor to strong perturbations of nearly any type. We will show the effect of combining different degradations in the next section.

To finish this section, let us mention that we conducted similar experiments in 3D. We used oblate ($\sigma_1 = \sigma_2 = 1$ and $\sigma_3 = 1/2$) or prolate ($\sigma_1 = 1$ and $\sigma_2 = \sigma_3 = 1/2$) ellipsoids. We do not include the results here due to space limitations. The conclusions obtained in 2D are still valid in 3D: the structure tensor is robust to anisotropy, deformation, resolution and noise. It is slightly less robust to blur and texture but sufficiently to analyse significantly degraded images. This will be illustrated in the next section.

III. ANALYZING TUMOR SPHEROIDS

In this section, we conduct numerical experiments to evaluate the structure tensor performance on synthetic and real data. The main biological problem addressed in our experiments is the analysis of geometrical configurations of nuclei in multicellular tumor spheroids. There are at least two reasons making this analysis relevant. First, tumor development is associated with a disorganization of the tissue. The role played by this disorganization is not well understood yet and it has been shown that it could have an impact on tumor cell behavior [46]. Second, among the key parameters involved in tumor growth, those related to mechanical forces seem to play a critical role [10], [29],
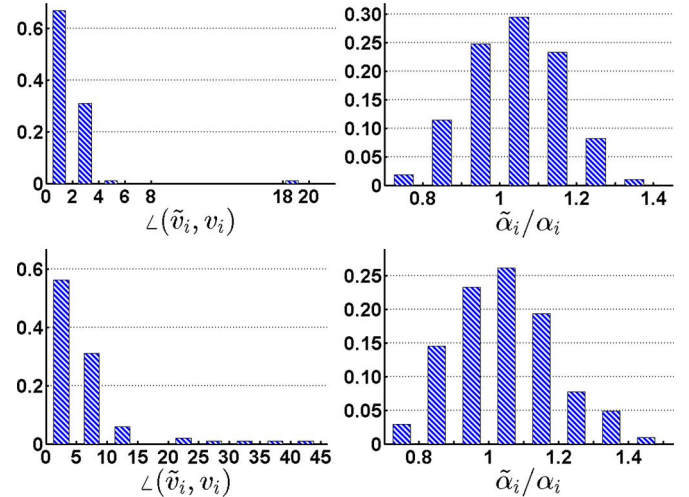

Fig. 7. Analysis of structure tensor based accuracy for the 2D test case. Histograms of orientations errors (left) and of anisotropy errors (right) for the clean (top) and degraded (bottom) images.

[40]. The elongation of nuclei in a preferential direction is an indicator of local stresses [16], [42]. Assessing the anisotropy and orientation of nuclei in their micro-environment is therefore crucial to better understand tumor organization and mechanics.

A. 2D and 3D Synthetic Data

In order to validate the theory, we first concentrate on 2D and 3D synthetic tumor spheroids, see Figs. 6(a) and 8(a)–(b). The way spheroid images are generated is described precisely in Appendix A. We denote $\mathbf{x}_i^c$ the center of the i-th nucleus. Its anisotropy is denoted α_i and defined as the ratio between the smallest and the largest axes lengths. Its main orientation is defined by a vector $\mathbf{v}_i \in \mathbb{R}^d$.

1) Measuring the Performance: In order to assess the structure tensor efficiency, we evaluate the following quantities:

- **Orientation.** Let $\tilde{\mathbf{v}}_i$ denote the eigenvector corresponding to the largest eigenvalue of $J_\rho(\mathbf{x}_i^c)$ and $\mathbf{v}_i = (\cos\theta_i, \sin\theta_i)$ denote the ground truth orientation. The following angles

$$\angle(\tilde{\mathbf{v}}_i, \mathbf{v}_i), \ i = 1, 2, \ldots, N, \qquad (8)$$

are used to evaluate the orientation accuracy in 2D. An angle close to $0°$ indicates a good orientation estimation, while an angle close to $90°$ is the worst possible estimate. For the 3D case, we choose for $\tilde{\mathbf{v}}_i$ either the largest eigenvector (prolate spheroid) or the smallest eigenvector (oblate spheroid).

- **Anisotropy.** The structure tensor based anisotropy is defined by $\tilde{\alpha}_i = ((\lambda_{\min}(J_\rho(\mathbf{x}_i^c)))/(\lambda_{\max}(J_\rho(\mathbf{x}_i^c))))^{1/2}$. The ratios

$$\tilde{\alpha}_i/\alpha_i, \quad i = 1, 2, \ldots, N, \qquad (9)$$

are used to quantify the estimated anisotropy accuracy, where α_i is the ground truth anisotropy. A ratio close to 1 indicates that the anisotropy is correctly evaluated.

Note that the orientation and anisotropy are evaluated at the centers of the nuclei $\mathbf{x}_i^c$ (which are known for synthetic data), while the matrix field $\bar{A}(\mathbf{x})$ is defined at every point $\mathbf{x}$ of the domain.
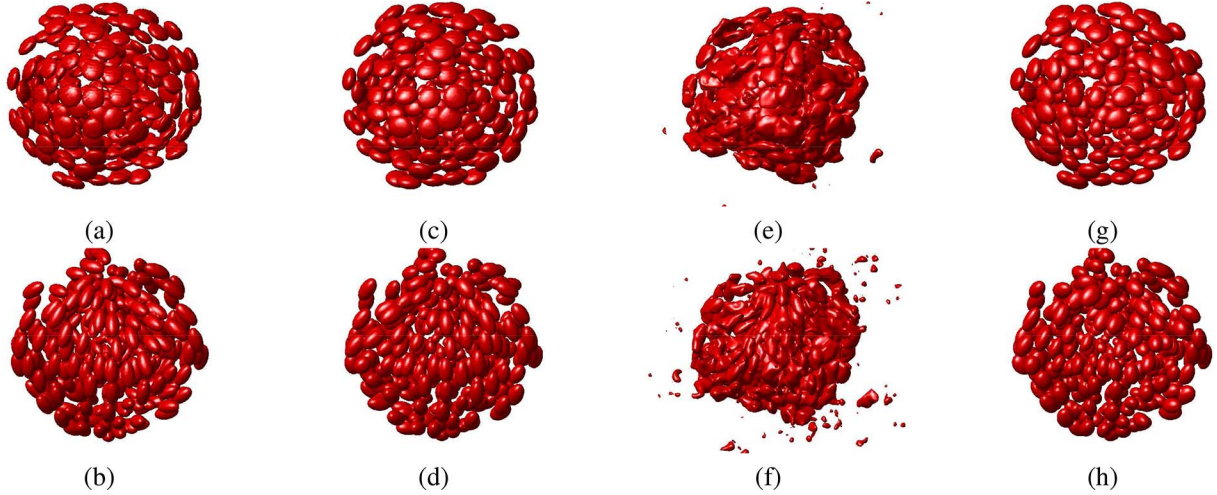
Fig. 8. 3D synthetic data (size: $128 \times 128 \times 128$). (a) spheroid with $\sigma_1 : \sigma_2 : \sigma_3 = 5 : 5 : 2$. (b) spheroid with $\sigma_1 : \sigma_2 : \sigma_3 = 5 : 2 : 2$. (c)–(d) structure tensor recomposition of the isosurfaces from the clean image. (e)–(f) isosurfaces of the degraded image in (a)–(b). (g)–(h) structure tensor recomposition of the isosurfaces from the degraded image.
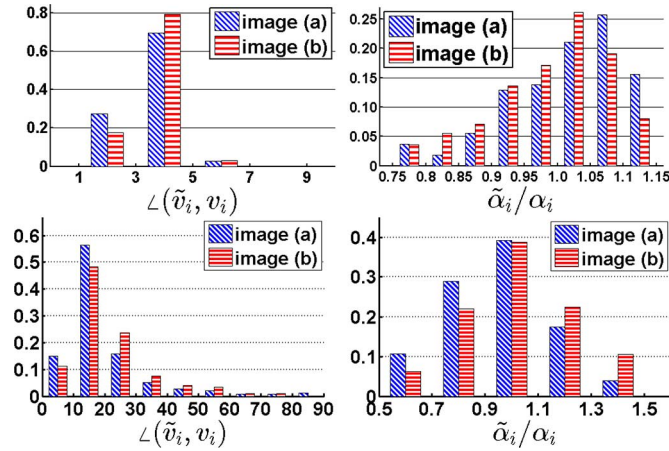

Fig. 9. Analysis of structure tensor based errors for the 3D test case. Histograms of orientations errors (left) and anisotropy errors (right) for the clean (top) and noisy (bottom) images. Image (a) is presented in Fig. 8(a) for the clean case and (e) for the noisy case, image (b) is presented in Fig. 8(b) for the clean case and (f) for the noisy case.

2) 2D Synthetic Data: We report numerical results on the 2D synthetic spheroid displayed in Fig. 6(a)–(b).

We use the value $\rho = 15$ in (3). This value is to be compared with the small axis of the ellipses that is $\sigma_1 = 10$ and the large axis σ_2 which ranges from 10 to 32. An adequate value for ρ is in the range $[R/2, 2R]$, where R denotes the diameter of the objects of interest. Fig. 6(b) shows the degraded spheroid. Here the degradation is composed of blur, deformation and texture (i.e., the worst effects studied previously). To show the structure tensor results, we plot an ellipse above the clean image at each cell center $\mathbf{x}_i^c$. Its radius is fixed by the ground truth since this feature is not recovered by the structure tensor. Its orientation and anisotropy are determined by the structure tensor. The resulting images are displayed in 6(c)–(d).

The orientations are well estimated even in the very degraded regime. The anisotropy is near perfectly recovered in the non noisy case. This is somehow surprising since for this image, only a small number of cells share the same orientation and anisotropy locally. This favorable behavior is another illustra-

tion of the fast convergence speed obtained in Theorem 1. The anisotropy is also quite well estimated in the very degraded regime, showing a remarkable robustness of the structure tensor.

To further quantify the accuracy of the results, the quantities (8)–(9) are evaluated. The histograms of both quantities are displayed in Fig. 7. For the clean image, approximately 95% of estimated orientations have an angular error below $4°$. Similarly, approximately 65% of estimated anisotropies have an error below 10%. For the degraded image, 85% of estimated orientations have an angular error below $10°$ and 65% of the anisotropies have an error below 20%. Those results are remarkable given the amount of degradation.

3) 3D Synthetic Data: We now test the structure tensor efficiency on 3D synthetic data, see Fig. 8(a) for an oblate example and (b) for a prolate example. The synthetic images have size $128 \times 128 \times 128$ with isotropic resolution. The images are composed of approximately 300 cells. The large axes of the ellipses are approximately 9 pixels long. The structure tensor J_ρ is computed with $\rho = 8$.

Similarly to the previous paragraph, we can recompose an ellipsoids field from the structure tensor and compare it to the ground truth. In Fig. 8(c)–(d), we recompose the ellipsoids by applying the structure tensor to the clean image. The result is visually satisfactory. The histograms of errors are shown in Fig. 9. As can be seen all orientations are evaluated with an error below $7°$. Similarly, 80% of the anisotropies are estimated with less than 10% error.

In Fig. 8(e)–(f), we display the isosurfaces of a degraded image. In Fig. 8(g)–(h), we show an ellipsoids field obtained by applying the structure tensor to the noisy image. Once again, the results are visually satisfactory: the structure tensor was able to recompose a field of ellipsoids similar to the clean image despite a severe degradation. This time, 80% of the orientations are estimated with an error below $30°$ while 90% of the anisotropies are estimated with less than 30% error. This is quite remarkable given the large deformations.

Overall, these results confirm that the structure tensor is an attractive tool to estimate anisotropies and orientations for 3D data.
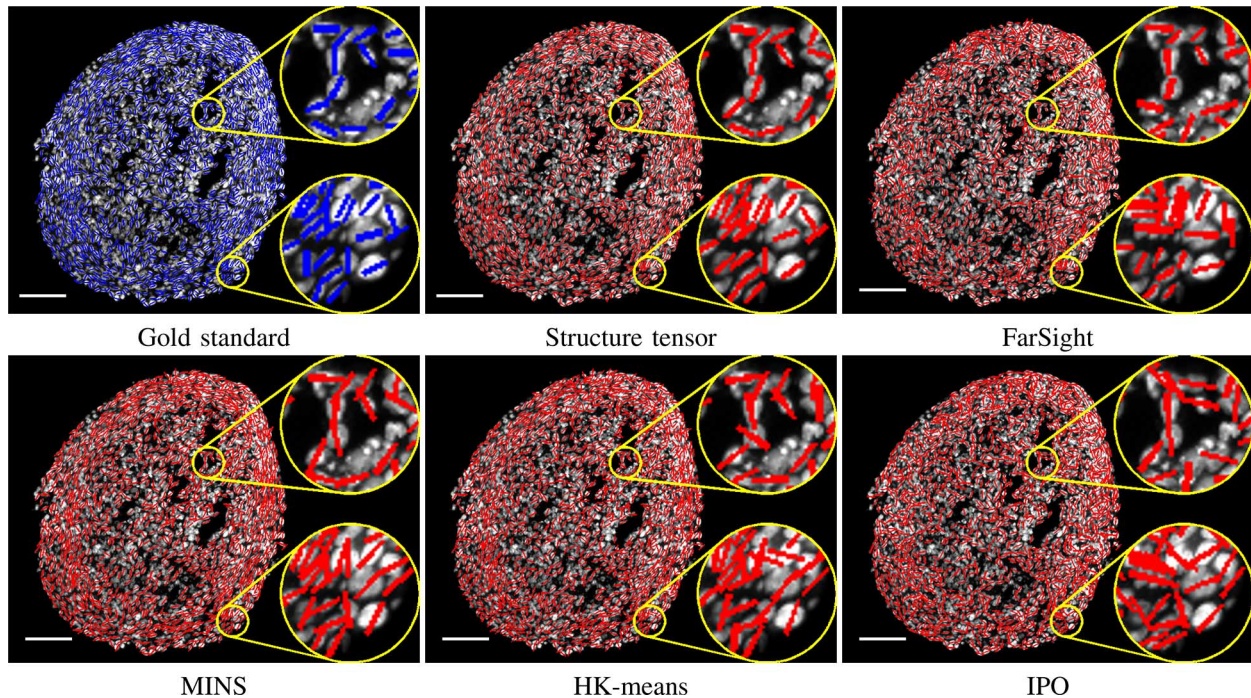
Fig. 10. Estimated orientations by different methods. Nuclei are stained using DAPI. Images were acquired using epifluorescence microscope (LEICA DM5000) and 10X objective NA: 0.3. Scale bar: 100 μm.

B. Performance Evaluation on Real Spheroid Images

We now evaluate the structure tensor estimates of orientation and anisotropy on a 2D real image. The image used in our experiment is displayed in Fig. 10(a) and contains 1465 nuclei. The gold standard reference consists of an ellipse approximating each distinguishable cell. It was obtained manually using Fiji. Let us emphasize that the gold standard is imprecise since i) a preferential orientation cannot be defined properly on isotropic cells and ii) fitting a thousand ellipses manually is subject to errors. Moreover, real data strongly depart from the ideal models considered in Section II since the nuclei may overlap in 2D.

The scalar ρ is set to 10 in this section. This value is selected manually and roughly corresponds to the mean radius of nuclei.

We compare the output of the structure tensor to a few state-of-the-art segmentation methods. We use the following softwares for comparisons: FarSight [27], the HK-means plugin from Icy [9], [33], the "IdentifyPrimaryObjects" (IPO) routine from Cellprofiler [7] and MINS [25].

Segmentation methods provide a more complete information than the structure tensor. To compare the output of segmentation methods with the structure tensor, we use the following methodology:

- Segment the object.
- Extract the segmentation connected components.
- For each element of the gold standard, find the closest segmented connected component. The chosen metric is the distance between barycenters.
- Approximate the closest connected component by an ellipse using a singular value decomposition.
- Retrieve the ratio between the eigenvalues and the leading eigenvector to obtain a measure of anisotropy and orientation from the segmentation.
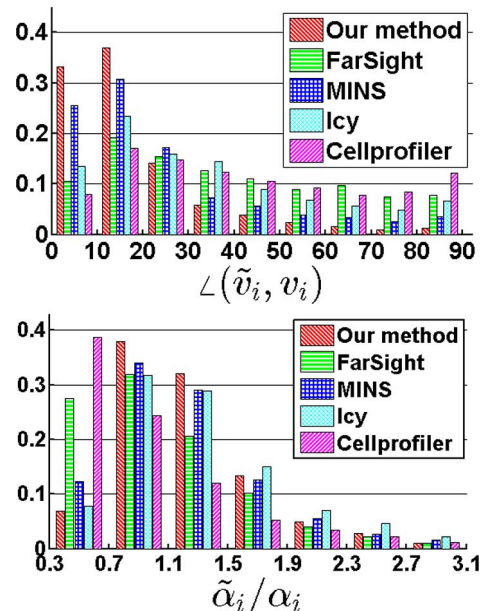

Fig. 11. Top: histogram of orientation error. Bottom: histogram of anisotropy error.

- Compare these features with the gold standard.

The experimental results are shown in Figs. 10 and 11. Despite the rather poor quality of data, the structure tensor results are remarkably accurate. More than 85% of the nuclei orientations are evaluated with an error no larger 20°, while the anisotropy seldom exceeds 50% error. Regarding the comparison with other methods, the graphs show that the structure tensor method provides better estimations of orientation and anisotropy than any of the tested segmentation algorithms. The best segmentation method for these quantitative criteria is MINS. It performs significantly worse than the structure tensor: 55% (in comparison to 85%) of the estimated orientations have
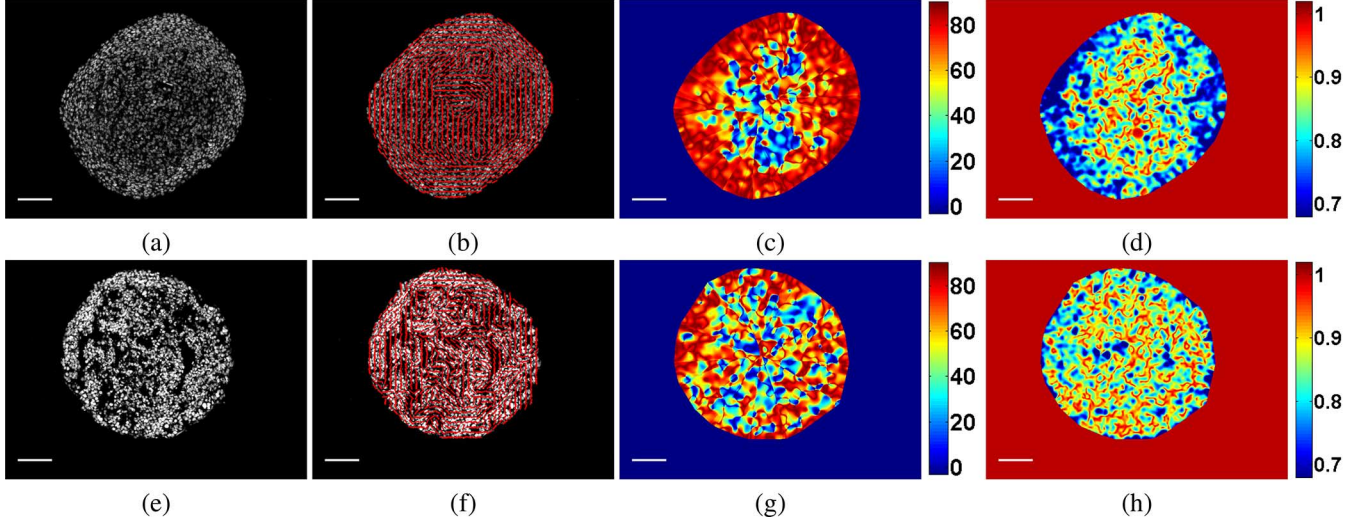
Fig. 12.   (a) and (e): images of Tumor spheroids cryosections with nuclei labelled using DAPI. Top row: control spheroid (with no drug). Bottom row: treated with latrunculin. (b) and (f): orientation map. (c) and (g): angle maps. An angle equal to 90° indicates that nuclei are aligned with the spheroid boundary. (d) and (h) anisotropy map. Images were acquired using epifluorescence microscope (LEICA DM5000) and 10X objective NA: 0.3. Scale bar: 100 μm.
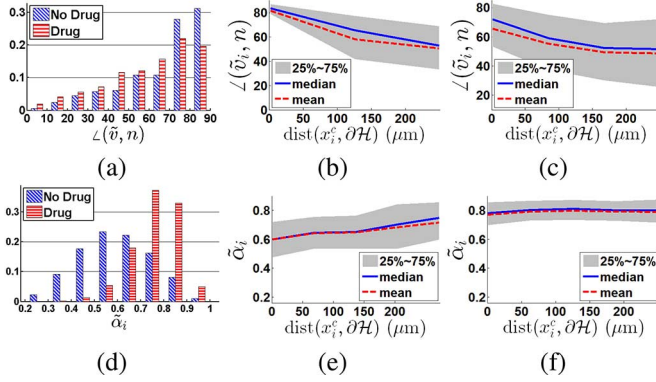

Fig. 13.   Structure tensor based orientations for the control and treated spheroids. (a) histogram of the orientation with respect to the normal at the closest point on the boundary. (b) and (c) distribution of orientations with respect to the distance to the boundary for the no-drug and drug cases respectively. (d) histograms of anisotropy. (e) and (f) distributions of anisotropies with respect to the distance to the boundary for the no-drug and drug cases respectively.

an error below 20°. The structure tensor anisotropies are also estimated slightly better than what is performed by MINS. The other methods really perform worse than the structure tensor. It can be seen in Fig. 10 that the orientations indeed seem much better recovered with the structure tensor.

C. Application to Drug Effects Analysis on Spheroids

As a proof of concept, spheroids were treated with latrunculin A, an inhibitor of actin polymerization. The visual comparison of (a) and (e) in Fig. 12 shows that this treatment induces a disorganization. We applied the structure tensor to extract the orientation and anisotropy maps in Fig. 12(c), (d), (g) and (h). The angle is measured with respect to the normal of the closest point of the boundary. In other words, an angle equal to 90° means that the local orientation is parallel to the boundary and an angle equal to 0° means that the local orientation is normal to the boundary.

The results obtained show a decrease of both nuclei anisotropy and alignment with the spheroid boundary in the outer layers after treatment. This observation is confirmed by the graphs showed in Fig. 13. In Fig. 13(a) we compare the alignment of the nuclei with respect to the boundary with or without treatment. In Fig. 13(b)–(c) we present the alignment with respect to the distance to the boundary. We observe that the mean angle at the origin is around 80° for the control spheroid and 60° for the treated spheroid, indicating that the drug tends to suppress the alignment of the nuclei with respect to the spheroid boundary. Moreover, in Fig. 13(b), the gray zone is narrow at the origin, reflecting the fact that nearly all nuclei are well aligned with the boundary in the outer layers. On the contrary, the gray zone at the origin of the graph in Fig. 13(c) is thick, indicating that the orientation is much more erratic.

In Fig. 13(d) we present the distribution of anisotropy for the control and the treated spheroid. In Fig. 13(e)–(f) we present the anisotropy with respect to the distance to the boundary. We observe that the mean anisotropy near the spheroid boundary is approximately equal to 0.6 for the control spheroid and 0.8 for the treated spheroid, indicating that nuclei are more round for the treated case.

As a summary, our methodology allows quantifying both the change of alignment and the decrease of anisotropy and could therefore have interesting applications in high content throughput.

IV. Conclusion & Outlook

We proposed an original theoretical analysis of structure tensors, justifying their use for evaluating orientations and anisotropies of cells or nuclei in 2D or 3D images. Our theoretical results were validated by numerical experiments, on synthetic and real data. Overall the present work shows that the structure tensor provides a fast, simple, robust, precise enough and user friendly method for biomedical imaging. It can be computed in near real-time and requires the tuning of a unique

parameter that has a simple physical interpretation. To finish, let us add a few remarks:

- First, cells or nuclei are not the only ellipsoid like objects and the method can be applied in any field where such objects appear (e.g., lobules in adipose tissues).
- Second, our results show that the structure tensor can be used as a rich source of information for segmentation methods. Knowing the rough orientation and anisotropy of a cell allows reducing the space of admissible segmentation shapes. For instance, it is fundamental to design good drawing distributions for methods based on marked point processes [32], [38].
- Finally, more and more mathematical models describe tissues as continuous media. The information contained in the structure tensor is itself continuous and therefore seems easy to use in data assimilation problems. This opens interesting perspectives to understand tissue biomechanics for instance. We plan to further investigate this problem in forthcoming works.

APPENDIX A
SYNTHESIZING IMAGES

In this section, we describe the way we generate synthetic images in the article.

The Givens transform, denoted by $R_{ij}^\theta \in \mathbb{R}^{d \times d}$, represents a counter-clockwise rotation for an angle θ in the (i, j)-coordinates plane. In the particular case $d = 2$, it is abbreviated R^θ. Given a vector $\mathbf{x} \in \mathbb{R}^d$, we let $\mathrm{diag}(\mathbf{x})$ denote a diagonal matrix with diagonal elements are the entries of $\mathbf{x}$. In what follows, $\varphi : \mathbb{R} \to \mathbb{R}$ is the bump function defined by

$$\varphi(t) = \begin{cases} \exp\left(-\frac{1}{1-t^2}\right), & \text{if } |t| < 1; \\ 0, & \text{otherwise.} \end{cases} \qquad (10)$$

A tumor spheroid image $u : \mathbb{R}^d \to \mathbb{R}_+$ is synthesized by

$$u(\mathbf{x}) = \sum_{i=1}^N \varphi\left((\mathbf{x} - \mathbf{x}_i^c)^T A_i (\mathbf{x} - \mathbf{x}_i^c)\right), \quad \forall \mathbf{x} \in \mathbb{R}^d, \qquad (11)$$

where N is the number of nuclei in the spheroid; φ is the bump function defined in (10); and $\mathbf{x}_i^c \in \mathbb{R}^d$ is the i-th nucleus center. The centers are drawn at random in a d-dimensional sphere in such a way that the nuclei do not overlap.

- If $d = 2$, the matrix $A_i \succ 0$ is defined by

$$A_i = R^{\theta_i} \mathrm{diag}(\sigma_{1,i}^{-2}, \sigma_{2,i}^{-2}) \left(R^{\theta_i}\right)^T. \qquad (12)$$

where R^{θ_i} is the Givens transform; θ_i is the phase angle of the radial line crossing the origin and the nucleus center $\mathbf{x}_i^c$.

- If $d = 3$, the matrix $A_i \succ 0$ is defined by

$$A_i = R_{1,2}^{\theta_i} R_{2,3}^{\gamma_i} \mathrm{diag}(\sigma_{1,i}^{-2}, \sigma_{2,i}^{-2}, \sigma_{3,i}^{-2})(R_{1,2}^{\theta_i} R_{2,3}^{\gamma_i})^T, \qquad (13)$$

where θ_i, γ_i denote the compass and elevation angles of the radial line crossing the ellipsoid center.

The anisotropy of the i-th nucleus is defined by

$$\alpha_i := \frac{\min\limits_{k=1,2,\ldots,d} \sigma_{k,i}}{\max\limits_{k=1,2,\ldots,d} \sigma_{k,i}}. \qquad (14)$$

In our 2D experiment, the anisotropy α_i increases linearly from the image center to the outer layers of the sphere. For the 3D case, the anisotropy α_i is set as constant. Figs. 6(a) and 8(a)–(b) display the 2D and 3D synthetic spheroids respectively.

APPENDIX B
PROOF OF THEOREMS AND PROPOSITIONS

A. Proof of Proposition 1

Elementary calculus leads to

$$\nabla \psi(\mathbf{x}) = 2\varphi'(\mathbf{x}^T A \mathbf{x}) A \mathbf{x}.$$

Therefore

$$\begin{aligned} J_\rho(0) &= \int_{\mathbb{R}^d} K_\rho(-\mathbf{x})(\nabla \psi \nabla \psi^T)(\mathbf{x}) \, d\mathbf{x} \\ &= 4A \left(\int_{\mathbb{R}^d} (\varphi'(\mathbf{x}^T A \mathbf{x}))^2 \mathbf{x}\mathbf{x}^T K_\rho(\mathbf{x}) \, d\mathbf{x}\right) A^T. \end{aligned}$$

If $\rho > \sqrt{d/2}$, then K_ρ is constant on the support of ψ. The change of variable $\mathbf{y} = \Sigma^{(1)/(2)} U^T \mathbf{x}$ leads to

$$J_\rho(0) = |\Sigma^{-\frac{1}{2}}| A U \Sigma^{-\frac{1}{2}} \underbrace{\left(\int_{\mathbb{R}^d} \varphi'(\|\mathbf{y}\|_2^2)^2 \mathbf{y}\mathbf{y}^T \, d\mathbf{y}\right)}_{\propto \mathrm{Id}} \Sigma^{-\frac{1}{2}} U^T A^T$$

$$\propto A.$$

Since K_ρ is constant on a neighborhood of the support of ψ, J_ρ is invariant by small translations hence J_ρ is locally constant around 0.

B. Proof of Proposition 2

We let $B(\mathbf{x}_0, \rho) = \{\mathbf{x} \mid \|\mathbf{x} - \mathbf{x}_0\|_2 \le \rho\}$ denote the Euclidian ball centered at $\mathbf{x}_0$ with radius ρ and $S(\mathbf{x}_0, \rho) = \{\mathbf{x} \mid \|\mathbf{x} - \mathbf{x}_0\|_2 = \rho\}$ the Euclidean sphere centered at $\mathbf{x}_0$ with radius ρ. We have

$$J_\rho(\mathbf{x}_0) = \frac{C_d}{\rho^d} \int_{B(\mathbf{x}_0, \rho)} (\nabla u \nabla u^T)(\mathbf{x}) \, d\mathbf{x}.$$

The image u is a sum of (non-overlapping) replicas of ψ. From Proposition 1, we know that all the replicas of ψ with support included in $B(\mathbf{x}_0, \rho)$ have a contribution to $J_\rho(\mathbf{x})$ proportional to A while the ones with support intersecting $S(\mathbf{x}_0, \rho)$ have a contribution that can be considered as a bias, with components bounded by $\int_{\mathbb{R}^d} |\partial_i \psi \partial_j \psi|(\mathbf{x}) \, d\mathbf{x}$. Let $\mathcal{I} = \{i \in \mathbb{Z}^d \mid \mathrm{supp}(\psi(\cdot - i)) \subset B(\mathbf{x}_0, \rho)\}$ and $\mathcal{J} = \{j \in \mathbb{Z}^d \mid \mathrm{supp}(\psi(\cdot - j)) \cap S(\mathbf{x}_0, \rho) \ne \emptyset\}$. For sufficiently large ρ, $|\mathcal{I}|$ scales as ρ^d (the volume of a ball of radius ρ) while $|\mathcal{J}|$ scales as ρ^{d-1} (the area of the sphere). Therefore $J_\rho(\mathbf{x}_0)$ behaves as $\rho \to \infty$ like

$$(\rho^d A + \rho^{d-1} B_\rho)/\rho^d,$$

where B_ρ is some bias of bounded amplitude. This implies that

$$\|\bar{J}_\rho(\mathbf{x}_0) - \bar{A}\|_2 = \mathcal{O}(1/\rho).$$

C. Proof of Theorem 1

The non-smoothed structure tensor is defined by

$$
\begin{aligned}
J_0 &= \nabla u \nabla u^T \\
&= (\text{III} \star \nabla \psi) \cdot (\text{III} \star \nabla \psi)^T \\
&= ((\partial_i \psi \partial_j \psi) \star \text{III})_{i,j},
\end{aligned}
$$

where the last equality follows from the fact that the functions are nonoverlapping. By exploiting the facts that $J_\rho = K_\rho \star J_0$ and $\widehat{\text{III}} = \text{III}$, it comes that

$$
\begin{aligned}
\hat{J}_\rho &= \left((\widehat{\partial_i \psi \partial_j \psi}) \cdot \widehat{\text{III}} \cdot \widehat{K}_\rho \right)_{1 \le i,j \le d} \\
&= \left(\sum_{k \in \mathbb{Z}^d} (\widehat{\partial_i \psi \partial_j \psi})(k) \widehat{K}_\rho(k) \delta_k \right)_{1 \le i,j \le d}.
\end{aligned}
$$

This provides a Fourier series decomposition of J_ρ:

$$
J_\rho(\mathbf{x}) = \left(\sum_{k \in \mathbb{Z}^d} (\widehat{\partial_i \psi \partial_j \psi})(k) \widehat{K}_\rho(k) \exp(-2i\pi \langle \mathbf{x}, k \rangle) \right)_{1 \le i,j \le d}.
$$

Moreover (1)—(ii) of the article implies that $\widehat{K}_\rho(0) = 1$, and for all i, j:

$$
\begin{aligned}
&\left| (J_\rho(\mathbf{x}))_{i,j} - (\widehat{\partial_i \psi \partial_j \psi})(0) \right| \\
&= \left| \sum_{k \in \mathbb{Z}^d \setminus \{0\}} (\widehat{\partial_i \psi \partial_j \psi})(k) \widehat{K}_\rho(k) \exp(-2i\pi \langle \mathbf{x}, k \rangle) \right| \\
&\le \sum_{k \in \mathbb{Z}^d \setminus \{0\}} \left| (\widehat{\partial_i \psi \partial_j \psi})(k) \right| \left| \widehat{K}_\rho(k) \right|
\end{aligned}
$$

By denoting $\mathbf{y} = \Sigma^{(1)/(2)} U^T \mathbf{x}$, we obtain:

$$
\begin{aligned}
&\left((\widehat{\partial_i \psi \partial_j \psi})(0) \right)_{1 \le i,j \le d} \\
&= \left(\int_{\mathbb{R}^d} (\partial_i \psi \partial_j \psi)(\mathbf{x}) \right)_{1 \le i,j \le d} \\
&= 4A \left(\int_{\mathbb{R}^d} \varphi'(\mathbf{x}^T A \mathbf{x})^2 \mathbf{x} \mathbf{x}^T \, d\mathbf{x} \right)_{1 \le i,j \le d} A^T \\
&= 4|\Sigma^{-\frac{1}{2}}| A U \Sigma^{-\frac{1}{2}} \\
&\quad \times \underbrace{\left(\int_{\mathbb{R}^d} \varphi'(\|\mathbf{y}\|_2^2) \mathbf{y} \mathbf{y}^T \, dx \right)_{1 \le i,j \le d}}_{\propto \text{Id}} \Sigma^{-\frac{1}{2}} U^T A^T \\
&\propto A.
\end{aligned}
$$

Since $\psi \in \mathcal{C}^1$ with bounded support, $c = \|\partial_i \psi \partial_j \psi\|_1 < +\infty$. Therefore $\|\widehat{\partial_i \psi \partial_j \psi}\|_\infty \le c$. Moreover, $\widehat{K}_\rho(k) = \widehat{K}(\rho k)$ so that

$$
\begin{aligned}
&\sum_{k \in \mathbb{Z}^d \setminus \{0\}} \left| (\widehat{\partial_i \psi \partial_j \psi})(k) \right| \left| \widehat{K}_\rho(k) \right| \\
&\le c \sum_{k \in \mathbb{Z}^d \setminus \{0\}} |\widehat{K}_\rho(k)| \\
&= c \sum_{k \in \mathbb{Z}^d \setminus \{0\}} |\widehat{K}(\rho k)| \\
&= c \sum_{k \in \mathbb{Z}^d \setminus \{0\}} \exp\left(-\rho^2 \|k\|_2^2 / 2 \right).
\end{aligned}
$$

We now remark that

$$
\begin{aligned}
&\sum_{k \in \mathbb{Z}^d} \exp\left(-\rho^2 \|k\|_2^2 / 2 \right) \\
&= \left(\sum_{j \in \mathbb{Z}} \exp\left(-\rho^2 j^2 / 2 \right) \right)^d \\
&= \left(1 + 2 \sum_{j \ge 1} \exp\left(-\rho^2 j^2 / 2 \right) \right)^d \\
&= (1 + 2u(\rho))^d \\
&= 1 + 2d u(\rho) + o_{\rho \to +\infty}(u(\rho))
\end{aligned}
$$

where

$$
\begin{aligned}
u(\rho) &= \sum_{j \ge 1} \exp(-\rho^2 j^2 / 2) \\
&\le \sum_{j \ge 1} \exp(-\rho^2 j / 2) = \frac{\exp(-\rho^2 / 2)}{1 - \exp(-\rho^2 / 2)}.
\end{aligned}
$$

Therefore $u(\rho)$ is asymptotic to $\exp(-\rho^2 / 2)$ when $\rho \to \infty$ and the claim follows.

D. Proof of Theorem 2

Let us denote $u' = u \circ F$ where F is a diffeomorphism such that $F = Id + G$, and $\|G\|_{W^{1,\infty}} \le \eta$. We also assume that ∇u is L-lipschitz and bounded uniformly: $\|\nabla u\|_\infty \le M$. We fix the scale ρ and denote for simplicity $K = K_\rho$. For every $\mathbf{y} \in \Omega$ we have $\nabla u(F(\mathbf{y})) = \nabla u(\mathbf{y}) + \mathbf{v}(\mathbf{y})$ where $\|\mathbf{v}(\mathbf{y})\|_2 \le L\|G(\mathbf{y})\|_2 \le L\eta$. Then

$$
J(\mathbf{x}) = \int_\Omega \nabla u(\mathbf{y}) \nabla u(\mathbf{y})^T K(\mathbf{x} - \mathbf{y}) d\mathbf{y},
$$

and by the chain rule we have (we denote for brevity $\mathbf{y}' = F(\mathbf{y})$)

$$
\begin{aligned}
J'(\mathbf{x}) &= \int_\Omega \nabla u'(\mathbf{y}) \nabla u'(\mathbf{y})^T K(\mathbf{x} - \mathbf{y}) d\mathbf{y} \\
&= \int_\Omega DF^T(\mathbf{y}') \nabla u(\mathbf{y}') \nabla u(\mathbf{y}')^T DF(\mathbf{y}') K(\mathbf{x} - \mathbf{y}) d\mathbf{y}.
\end{aligned}
$$

By expanding the product in the integral, we obtain:

$$
J'(\mathbf{x}) = J(\mathbf{x}) + R(\mathbf{x}),
$$

where the remainder $R(\mathbf{x})$ satisfies

$$\|R(\mathbf{x})\|_2 \leq \eta \left[M^2(2 + \eta) + 2ML + L^2 \right]$$

which proves the claim.

ACKNOWLEDGMENT

REFERENCES

[1] D. Ambrosi and F. Mollica, "On the mechanics of a growing tumor," *Int. J. Eng. Sci.*, vol. 40, no. 12, pp. 1297–1316, 2002.

[2] J. Bigun, G. H. Granlund, and J. Wiklund, "Multidimensional orientation estimation with applications to texture analysis and optical flow," *IEEE Trans. Pattern Anal. Mach. Intell.*, vol. 13, no. 8, pp. 775–790, Aug. 1991.

[3] I. Bonnet et al., "Mechanical state, material properties and continuous description of an epithelial tissue," *J. R. Soc. Interface*, vol. 9, pp. 2614–2623, 2012.

[4] R. N. Bracewell, *The Fourier Transform and its Applications*. New York: McGraw-Hill, 1978.

[5] D. Bresch et al., "A viscoelastic model for avascular tumor growth," *Discrete Continuous Dynamical Syst.*, pp. 101–108, 2009.

[6] A. Buades, B. Coll, and J.-M. Morel, "A non-local algorithm for image denoising," in *Proc. IEEE Comput. Soc. Comput. Vis. Pattern Recognit.*, 2005, vol. 2, pp. 60–65.

[7] A. E. Carpenter et al., "Cellprofiler: Image analysis software for identifying and quantifying cell phenotypes," *Genome Biol.*, vol. 7, no. 10, p. R100, 2006.

[8] K. Dabov, A. Foi, V. Katkovnik, and K. Egiazarian, "Image denoising by sparse 3-d transform-domain collaborative filtering," *IEEE Trans. Image Process.*, vol. 16, no. 8, pp. 2080–2095, Aug. 2007.

[9] F. De Chaumont et al., "Icy: An open bioimage informatics platform for extended reproducible research," *Nature Methods*, vol. 9, no. 7, pp. 690–696, 2012.

[10] A. Desmaison, C. Frongia, K. Grenier, B. Ducommun, and V. Lobjois, "Mechanical stress impairs mitosis progression in multi-cellular tumor spheroids," *PloS One*, vol. 8, no. 12, p. e80447, 2013.

[11] S. Federico and T. C. Gasser, "Nonlinear elasticity of biological tissues with statistical fibre orientation," *J. R. Soc. Interface*, vol. 7, no. 47, pp. 955–966, 2010.

[12] J. Fehrenbach, P. Weiss, and C. Lorenzo, "Variational algorithms to remove stationary noise: Applications to microscopy imaging," *IEEE Trans. Image Process.*, vol. 21, no. 10, pp. 4420–4430, Oct. 2012.

[13] E. Fonck et al., "Effect of aging on elastin functionality in human cerebral arteries," *Stroke*, vol. 40, no. 7, pp. 2552–2556, 2009.

[14] W. Förstner and E. Gülch, "A fast operator for detection and precise location of distinct points, corners and centres of circular features," in *Proc. ISPRS Intercommission Conf. Fast Process. Photogrammetric Data*, 1987, pp. 281–305.

[15] G. H. Granlund and H. Knutsson, *Signal Processing for Computer Vision*. New York: Springer, 1995, vol. 2.

[16] F. Guilak, "Compression-induced changes in the shape and volume of the chondrocyte nucleus," *J. Biomechan.*, vol. 28, no. 12, pp. 1529–1541, 1995.

[17] C. Harris and M. Stephens, "A combined corner and edge detector," in *Alvey Vis. Conf.*, Manchester, U.K., 1988, vol. 15, p. 50.

[18] J. Humphrey, "Review paper: Continuum biomechanics of soft biological tissues," *Proc. R. Soc. London*, ser. Math., Phys. Eng. Sci., vol. 459, no. 2029, pp. 3–46, 2003.

[19] J. Humphrey and K. Rajagopal, "A constrained mixture model for growth and remodeling of soft tissues," *Math. Models Methods Appl. Sci.*, vol. 12, no. 03, pp. 407–430, 2002.

[20] B. Jähne, *Spatio-Temporal Image Processing: Theory and Scientific Applications*. New York: Springer Science Business Media, 1993, vol. 751.

[21] B. Jähne, *Digital Image Processing: Concepts, Algorithms, and Scientific Applications*, 4th ed. New York: Springer, 1997.

[22] R. Jorand et al., "Deep and clear optical imaging of thick inhomogeneous samples," *PloS One*, vol. 7, no. 4, 2012.

[23] T. Lindeberg, *Scale-Space Theory in Computer Vision*. New York: Springer Science Business Media, 2013, vol. 256.

[24] T. Lindeberg and J. Gårding, "Shape-adapted smoothing in estimation of 3-d shape cues from affine deformations of local 2-d brightness structure," *Image Vis. Comput.*, vol. 15, no. 6, pp. 415–434, 1997.

[25] X. Lou, M. Kang, P. Xenopoulos, S. Munoz-Descalzo, and A.-K. Hadjantonakis, "A rapid and efficient 2d/3d nuclear segmentation method for analysis of early mouse embryo and stem cell image data," *Stem Cell Rep.*, vol. 2, no. 3, pp. 382–397, 2014.

[26] B. D. Lucas and T. Kanade, "An iterative image registration technique with an application to stereo vision," in *IJCAI*, 1981, vol. 81, pp. 674–679.

[27] J. Luisi, A. Narayanaswamy, Z. Galbreath, and B. Roysam, "The farsight trace editor: An open source tool for 3-d inspection and efficient pattern analysis aided editing of automated neuronal reconstructions," *Neuroinformatics*, vol. 9, no. 2, pp. 305–315, 2011.

[28] A. Menzel, M. Harrysson, and M. Ristinmaa, "Towards an orientation-distribution-based multi-scale approach for remodelling biological tissues," *Comput. Methods Biomechan. Biomed. Eng.*, vol. 11, no. 5, pp. 505–524, 2008.

[29] F. Montel et al., "Stress clamp experiments on multicellular tumor spheroids," *Phys. Rev. Lett.*, vol. 107, no. 18, p. 188102, 2011.

[30] N. Olivier et al., "Cell lineage reconstruction of early zebrafish embryos using label-free nonlinear microscopy," *Science*, vol. 329, no. 5994, pp. 967–971, 2010.

[31] K. Palaniappan, I. Ersoy, and S. K. Nath, "Moving object segmentation using the flux tensor for biological video microscopy," in *Advances in Multimedia Information Processing-PCM 2007*. New York: Springer, 2007, pp. 483–493.

[32] G. Perrin, X. Descombes, and J. Zerubia, "A marked point process model for tree crown extraction in plantations," in *Proc. IEEE Int. Conf. Image Process.*, 2005, vol. 1, pp. I–661.

[33] S. Pop et al., "Extracting 3d cell parameters from dense tissue environments: Application to the development of the mouse heart," *Bioinformatics*, vol. 29, no. 6, pp. 772–779, 2013.

[34] A. R. Rao and B. G. Schunck, "Computing oriented texture fields," *CVGIP: Graphical Models Image Process.*, vol. 53, no. 2, pp. 157–185, 1991.

[35] R. Rezakhaniha et al., "Experimental investigation of collagen waviness and orientation in the arterial adventitia using confocal laser scanning microscopy," *Biomechan. Model. Mechanobiol.*, vol. 11, no. 3–4, pp. 461–473, 2012.

[36] L. I. Rudin, S. Osher, and E. Fatemi, "Nonlinear total variation based noise removal algorithms," *Physica D, Nonlinear Phenomena*, vol. 60, no. 1, pp. 259–268, 1992.

[37] H. Scharr, S. Körkel, and B. Jähne, "Numerische isotropieoptimierung von fir-filtern mittels querglättung," in *Mustererkennung 1997*. New York: Springer, 1997, pp. 367–374.

[38] E. Soubies, P. Weiss, and X. Descombes, "A 3d segmentation algorithm for ellipsoidal shapes. application to nuclei extraction," in *Proc. ICPRAM*, 2013.

[39] J.-L. Starck, E. J. Candès, and D. L. Donoho, "The curvelet transform for image denoising," *IEEE Trans. Image Process.*, vol. 11, no. 6, pp. 670–684, Jun. 2002.

[40] T. Stylianopoulos et al., "Causes, consequences, and remedies for growth-induced solid stress in murine and human tumors," *Proc. Nat. Acad. Sci.*, vol. 109, no. 38, pp. 15101–15108, 2012.

[41] D. Tschumperlé, "Fast anisotropic smoothing of multi-valued images using curvature-preserving pde's," *Int. J. Comput. Vis.*, vol. 68, no. 1, pp. 65–82, 2006.

[42] M. Versaevel, T. Grevesse, and S. Gabriele, "Spatial coordination between cell and nuclear shape within micropatterned endothelial cells," *Nature Commun.*, vol. 3, p. 671, 2012.

[43] J. Weickert, *Anisotropic Diffusion in Image Processing*. Stuttgart, Germany: Teubner, 1998, vol. 1.

[44] J. Weickert, "Coherence-enhancing diffusion filtering," *Int. J. Comput. Vis.*, vol. 31, no. 2–3, pp. 111–127, 1999.

[45] J. Weickert and H. Scharr, "A scheme for coherence-enhancing diffusion filtering with optimized rotation invariance," *J. Vis. Commun. Image Represent.*, vol. 13, no. 1, pp. 103–118, 2002.

[46] B. Weigelt and M. J. Bissell, "Unraveling the microenvironmental influences on the normal mammary gland and breast cancer," in *Seminars in Cancer Biology*. New York: Elsevier, 2008, vol. 18, pp. 311–321.